Received: 2 July 2019 | Revised: 8 August 2019 | Accepted: 16 August 2019

DOI: 10.1002/aoc.5229

FULL PAPER

WILEY Applied Organometallic Chemistry

Pd@tetrahedral hollow magnetic nanoparticles coated with N-doped porous carbon as an efficient catalyst for hydrogenation of nitroarenes

Samahe Sadjadi[1] | **Majid M. Heravi**[2]

[1]Gas Conversion Department, Faculty of Petrochemicals, Iran Polymer and Petrochemicals Institute, 15km Tehran-Karaj Highway, Pajuhesh Science and Technology Park,Pajuhesh Boulevard PO Box 14975-112, Tehran, Iran

[2]Department of Chemistry, School of Science, Alzahra University, PO Box 1993891176, Vanak, Tehran, Iran

Correspondence
Samahe Sadjadi, Gas Conversion Department, Faculty of Petrochemicals, Iran Polymer and Petrochemicals Institute,15km Tehran-Karaj Highway, Pajuhesh Science and Technology Park, Pajuhesh Boulevard PO Box 14975-112, Tehran, Iran.
Email: samahesadjadi@yahoo.com; s.sadjadi@ippi.ac.ir

Majid M. Heravi, Department of Chemistry, School of Science, Alzahra University, PO Box 1993891176, Vanak, Tehran, Iran.
Email: mmh1331@yahoo.com; mheravi.alzahra@ac.ir

Funding information
Iran National Science Foundation, Grant/Award Number: 97009384; the Iran Polymer and Petrochemical Institute and Alzahra University

Hollow magnetic nanoparticles (MNPs) with tetrahedral morphology were synthesized and then covered by a shell prepared by coating with melamine–formaldehyde followed by the introduction of glucose-derived carbon. Subsequently, Pd nanoparticles were immobilized and the core–shell nanocomposite was carbonized. The obtained magnetic catalyst was successfully applied for the hydrogenation of nitroarenes in aqueous media. To investigate the effects of the morphology of MNPs, the nature of carbon shell, and the order of incorporation of Pd nanoparticles, several control catalysts, including the MNPs with different morphologies (disc-like and cylinder); MNPs coated with different shells (sole glucose-derived carbon or melamine–formaldehyde carbon shell); and a nanocomposite, in which Pd was immobilized after carbonization, were prepared and examined as catalyst for the model reaction. To justify the observed different catalytic activities of the catalysts, their Pd loadings, leaching, and specific surface areas were compared. The results confirmed that tetrahedral MNPs coated with porous N-rich carbon shell exhibited the best catalytic activity. The high catalytic activity of this catalyst was attributed to its high surface area and the interaction of N-rich shell with Pd nanoparticles that led to the higher Pd loading and suppressed Pd leaching.

KEYWORDS
catalyst, hydrogenation, magnetic nanoparticles, N-doped carbon

1 | INTRODUCTION

In recent years, magnetic nanoparticles (MNPs) and their composites have attracted considerable attention[1] in nanotechnology, bioimaging, drug delivery, and heterogeneous catalysis due to their magnetic properties, large surface-to-volume ratio, and very active surface for the immobilization or adsorption of other functional groups.[2,3] Notably, the properties of MNPs are dependent on the size and the morphology of the nanoparticles. Among MNPs, maghemite nanoparticles (γ-Fe_2O_3), especially hollow structures,[4,5] are well-known paramagnetic materials, which have been widely used in catalysis because of their unique properties such as easy

preparation processes, facile separation, and environmental stability that provide facile recovery and recycling.[4,6,7]

Unfortunately, MNPs have a strong tendency to agglomerate because of their large surface area-to-volume ratio and also magnetic dipole–dipole interactions.[8] These drawbacks are the main challenges for the synthesis of stable magnetic nanocomposites with good dispersion. By contrast, in the case of loading of other nanoparticles on MNPs, the involvement of iron in the redox processes decreases the catalytic activity.[9] It is noticed that the coating of outer surface of the MNPs with inorganic or organic inert materials such as polymer, silica, or carbon can furnish a solution to this problem.[10]

Lately, given their widespread applications in numerous fields such as catalysis,[11] fuel cell,[12] gas storage, and separation,[13] porous carbon materials have received growing attention.[14,15] Porous carbons based on polymer are an attractive generation of porous materials created from light elements (H, B, C, N, and O) that are known to form strong covalent bonds.[16,17] General methods for the preparation of these carbons are based on the use of nitrogen precursors such as aniline,[18] pyrrole,[19] and acrylonitrile[20] that lead to the synthesis of N-doped porous carbons. Among available molecular monomers, melamine,[21,22] which is a cheap and abundant chemical with 66% N by mass, is recognized as an ideal candidate for the fabrication of N-doped porous carbons. Melamines have many advantages over conventional N-rich precursors due to their rigid molecular backbone, high nitrogen content, low density, and high thermal and/or chemical stability.[23] More importantly, the pore size of the melamine-derived carbons can be tuned by wise choice of monomer, controlling polymerization condition, etc.[24]

Anilines and their derivatives are key chemicals for the production of dyes, agricultural chemicals, pharmaceuticals, and biologically active materials.[25,26] By contrast, catalytic hydrogenation of nitroarene compounds is one of the most powerful tools for the excellent synthesis of primary amines. Importantly, about 85% of aniline is produced via the environmentally benign catalytic hydrogenation of nitrobenzene using gaseous hydrogen.[27] This chemical transformation has been promoted using a range of homogeneous and heterogeneous catalysts.[28–33] However, many of these catalytic systems have some limitations such as tedious and time-consuming workup processes, necessity of extra additives, and incomplete noble metal recovery from such complex systems. Hence, development of a facile, fast, and convenient method for the synthesis of aniline derivatives is of great importance.

Considering the importance of the morphology of MNPs and their coating with inert materials for the catalytic activity, herein, we aim to scrutinize the effects of the morphology of MNPs, the nature of a carbon shell on the periphery of MNPs, and the order of the immobilization of zero-valence Pd nanoparticles on the carbon-coated MNPs on the catalytic activity of the resulting catalysts for the hydrogenation of nitroarenes.

2 | EXPERIMENTAL

2.1 | Materials and instruments

All the chemicals and solvents including $FeCl_3{\cdot}6H_2O$, D-(+)-glucose, urea, melamine, formaldehyde, $NaBH_4$, Pd$(OAc)_2$, EtOH, deionized water, and toluene were purchased from Sigma-Aldrich, Germany-Taufkirchen and used as received. The hydrogenation reaction was performed using nitroarenes. All nitroarenes were of analytical grade, provided from Sigma-Aldrich, Germany-Taufkirchen, and used without further purification.

The formation of Pd@TH-Fe_2O_3@MFC as well as control samples was confirmed by applying Brunauer–Emmett–Teller (BET), vibrating-sample magnetometry (VSM), X-ray diffraction (XRD), thermogravimetric analysis (TGA), field emission scanning electron microscopic (FESEM)/energy-dispersive X-ray spectroscopy (EDS), Fourier-transform infrared (FTIR), transmission electron microscopy (TEM), Raman spectroscopy, and inductively coupled plasma (ICP) atomic emission spectroscopy. XRD patterns were obtained using a Siemens, D5000 diffractometer with Cu-K_α radiation at 60 KeV and 15 Ma. FESEM images of the catalyst and control samples were recorded on a MIRA 3 TESCAN-XMU instrument using Au-coated samples and an acceleration voltage of 20 Kv. TEM images of the catalyst were obtained using Philips CM30300Kv field emission transmission electron microscope. TGAs were carried out using a METTLER TOLEDO instrument under nitrogen atmosphere over the range of 40 to 800 °C with a heating rate of 10 °C min^{-1}. FTIR spectra were collected on a PERKIN-ELMER-Spectrum 65 FTIR spectrometer using KBr pellets. BET analyses were performed using a BELsorp Mini II instrument. The degassing process of samples was carried out at 423 K for 3 hr. The magnetic properties of the samples were estimated using VSM (Lakeshore7407) at room temperature. Teksan N1-541 spectrometer was used for recording Raman spectrum at $\lambda = 532$ nm. The ultrasonic apparatus employed for the synthesis of the catalyst was Bandelin HD 3200 with output power between 100 and 200 W and tip TT13. Using an ICP analyzer of type Varian Vista-pro, measurements of the Pd and Fe loading and leaching of the catalyst were performed.

2.2 | Synthesis of the catalyst

2.2.1 | Synthesis of nanomagnetic hollow tetrahedral Fe_2O_3 (TH-Fe_2O_3): Compound 1

Typically, to a solution of $FeCl_3{\cdot}6H_2O$ (10 mmol) in deionized water (65 mL), a solution of urea (16 mmol) in deionized water (60 mL) was added. The resulting mixture was then stirred vigorously. After 10 min, the reaction mixture was transferred into a Teflon-lined stainless-steel autoclave (150 mL capacity) and maintained at 200 °C for 8 hr. At the end of the hydrothermal process, the reactor was cooled down to room temperature and the MNPs were separated using an external magnet, washed with a mixture of deionized water–EtOH repeatedly, and dried at 100 °C for 12 hr in an oven.

2.2.2 | Synthesis of the TH-Fe_2O_3@MF core–shell: Compound 2

Initially, melamine (100 mg) and formaldehyde (40 mg) were mixed in 10 mL deionized water. Next, the pH of the mixture was adjusted to 8.0 by adding Na_2CO_3 solution. Under continuous magnetic stirring at 70 °C, pre-polymerization of melamine and formaldehyde began and continued for 1 hr. Then, TH-Fe_2O_3 (0.5 g) was dispersed in 10 mL deionized water. Subsequently, 100 mg formaldehyde was added and the pH of the mixture was adjusted to 9.0 by adding Na_2CO_3 solution. The mixture was then well-dispersed under ultrasonic irradiation for 1 hr. After sonication, the pre-polymer solution was mixed with the TH-Fe_2O_3 mixture. In the following steps, the pH of the mixture was adjusted to 5.0 by adding HCl aqueous solution. Then, the prepared mixture was transferred into a glass tube and heated to 120 °C and kept at this temperature for half an hour. Upon completion of the reaction, the reaction mixture was allowed to cool down to room temperature, and then magnetically separated. The TH-Fe_2O_3@MF was washed with a mixture of deionized water/EtOH repeatedly and dried at 100 °C for 10 hr to obtain pure product. The yield of this process was 75%.

2.2.3 | Preparation of TH-Fe_2O_3@MF-Glu core–shell: Compound 3

An aqueous solution of glucose (40 mL, 0.3 M) was prepared and then added to an aqueous suspension of TH-Fe_2O_3@MF (10 g L^{-1}). The mixture was thoroughly dispersed by sonication with power of 200 W for half an hour and then transferred into a Teflon-lined stainless steel autoclave and kept at 200 °C for 24 hr. At the end of the hydrothermal process, the reactor was cooled down to room temperature and the MNPs were magnetically separated, washed with a mixture of deionized water/EtOH, and dried at 60 °C for 12 hr.

2.2.4 | Immobilization of Pd NPs on the TH-Fe_2O_3@MF-Glu core–shell: Compound 4

The Pd@TH-Fe_2O_3@MF-Glu was synthesized by conventional impregnation-reduction method. Typically, TH-Fe_2O_3@MF-Glu (3 g) was stirred in toluene (40 mL) in a flask for half an hour. Then, a solution of Pd salt, $Pd(OAc)_2$, in toluene (40 mL, 0.01 M) was added under stirring condition for 6 hr. In the following steps, an aqueous solution of $NaBH_4$ in MeOH (15 mL, 0.2 N) that served as the reducing agent was added into the solution under N_2 atmosphere and then the resulting mixture was stirred vigorously for 2 hr. After magnetic separation, the solid product was washed with a mixture of deionized water/EtOH several times and then dried at 60 °C for 12 hr.

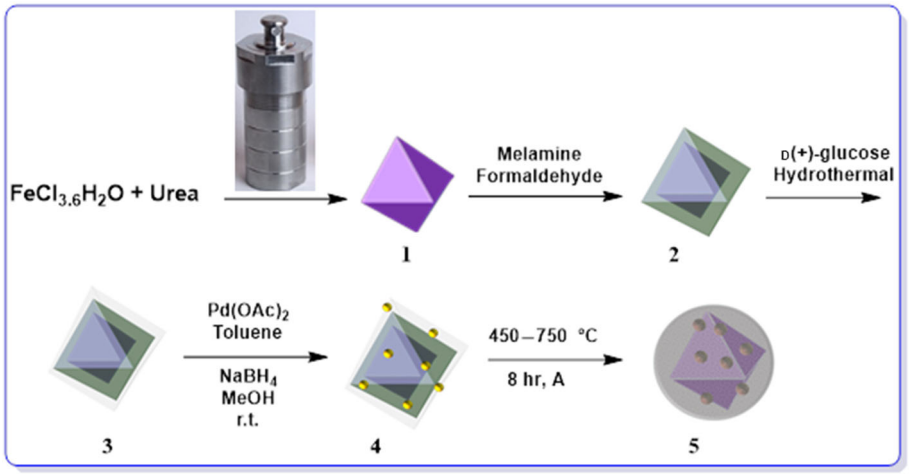

FIGURE 1 Schematic routes for the synthesis of Pd@TH-Fe_2O_3@MFC. r.t., room temperature

2.2.5 | Synthesis of Pd@TH-Fe_2O_3@MFC core–shell: Compound 5

To prepare palladated, magnetic, N-rich porous carbon core–shell system **5**, Pd@TH-Fe_2O_3@MF-Glu was carbonized at 450 °C with a heating rate of 3 °C min^{-1} for 7 hr in a tubular furnace under argon flow followed by the heat treatment at 750 °C for 1 hr. In Figure 1, the schematic procedure for the synthesis of catalyst 5 is depicted.

2.2.6 | Synthesis of control catalysts

To further examine the effect of different morphologies of MNPs and the carbon sources, several control catalysts, compounds **17, 9, 7, 11, 13, and 16**, were prepared and their catalytic activities were compared with that of compound **5**. Compound **8** was synthesized by using a similar procedure employed for the synthesis of compound **1**, except that a $FeCl_3{\cdot}6H_2O$:urea ratio of 10:12 (mmol/mmol) was applied instead of the ratio of 10:16.

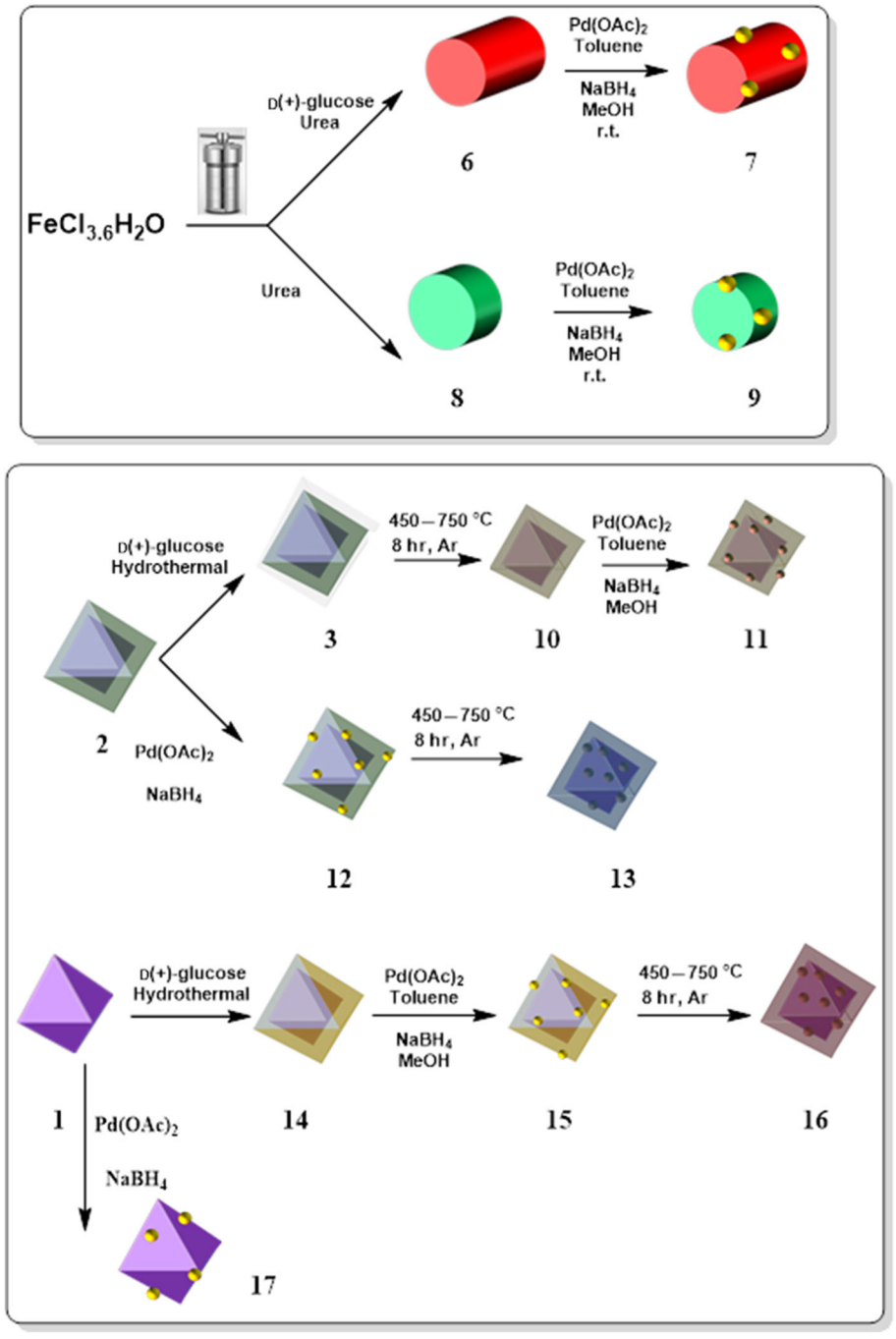

FIGURE 2 Schematic routes for the synthesis of the control catalysts. r.t., room temperature

Compound **6** was prepared using the same procedure used for compound **1**, except that glucose was also applied as one of the precursors. In this sample, the ratio of $FeCl_3 \cdot 6H_2O$:urea:glucose was 10:8:1.2 (mmol/mmol/mmol). Compounds **7** and **9** were produced by palladating compounds **6** and **8**, respectively. Compound **17** was synthesized by palladating compound **1**. The procedure for the immobilization of Pd nanoparticles was similar to the method used for the synthesis of catalyst **5**, except that different morphologies of bare h-Fe_2O_3 were used instead of TH-Fe_2O_3@MF-Glu. Compound **11** was also synthesized by immobilization of Pd nanoparticles on the surface of compound **10,** which was achieved through carbonization of compound **3**. To prepare compound **13,** compound **2** was successfully palladated and then carbonized. To synthesize compound **16**, the outer shell of compound **1** was directly covered by glucose, without using the melamine–formaldehyde polymeric shell, to furnish compound **14**. Next, the product (TH-Fe_2O_3-Glu) was palladated to form compound **15** and then carbonized through the similar carbonization procedure used for the synthesis of compound **5**. In Figure 2, the schematic procedures for the synthesis of the control catalysts are depicted.

2.2.7 | Hydrogenation of nitrobenzene

In a two-necked flask containing a solution of nitroarene (1 mmol in 5 mL of deionized water), Pd@TH-Fe_2O_3@MFC was added as a catalyst (1.2 mol%). Subsequently H_2 gas as a reducing agent was purged (1 atm.). The glass reactor was stirred vigorously (400 rpm) and the progress of the reduction reaction was then monitored via thin-layer chromatography using an *n*-hexane-to-ethyl acetate ratio of 9:1. Upon completion of the reaction, the reactor was cooled and Pd@TH-Fe_2O_3@MFC catalyst was separated using an external magnet. The recovered Pd@TH-Fe_2O_3@MFC was washed several times with a mixture of distilled water and EtOH, dried in oven, and reused for the next run. The resulting filtrate was collected and diluted with EtOH to obtain the final product. All the obtained products were identified and their formation was confirmed by FTIR spectroscopy.

3 | RESULTS AND DISCUSSION

3.1 | Investigation of the roles of MNPs morphology, nature of carbon shell carbon shell, and order of Pd immobilization in the catalytic activity: Selecting the most efficient catalyst

As mentioned, one of the aims of this research is investigation of the effect of the morphology of bare hollow MNPs on the catalytic activity. Hence, three different morphologies of hollow MNPs, namely, disc-like, cylinder, and tetrahedral (compounds 1, 8, and 6 in Figure 2), were simply prepared by altering the $FeCl_3 \cdot 6H_2O$:urea:glucose ratio and characterized by using FESEM analysis (Figure 3). As shown in Figure 3, the three targeted morphologies were successfully prepared. The EDS analyses also confirmed the success of the procedures for the synthesis of MNPs. Verifying the three morphologies, Pd nanoparticles were immobilized on the three as-prepared MNPs using a similar protocol (see the "Experimental" section). To elucidate whether the morphology of MNPs can affect the catalytic activity, the catalytic activities of three palladated MNPs (compounds 7, 9, and 17, Figure 2) for the hydrogenation of nitrobenzene as a model substrate were studied (Table 1). Prior to the hydrogenation test, the reaction condition was optimized (Table S1) by measuring the yield of the reaction using different solvents, temperatures, and catalyst loading. The highest yield of the product was achieved at room temperature in water using a 1.2 mol% catalyst. The results indicated that compound 17, the palladated tetrahedral MNPs, and compound 9, disc-like MNPs, showed the highest and the lowest catalytic activities, respectively. This result established that the morphology of the MNPs can effectively influence the catalytic activity. The higher catalytic activity of MNPs with tetrahedral morphology can be attributed to the presence of more angles in this morphology that can promote more Pd anchoring. To verify this assumption, the Pd loadings of compounds 7, 9, and 17 were estimated via ICP.

The results in Table 1 show that the contents of Pd in those samples decreased in an order similar to that of the catalytic activity (compound 17 > compound 7 > compound 9), indicating the role of the MNPs morphology in the Pd loading. To further investigate the origin of the higher catalytic activity of the tetrahedral MNPs, the specific surface area of three compounds 7, 9, and 17 were measured via BET. The results indicated higher specific surface area of compound 17 (Table 1). Considering all of these results, the superior catalytic activity of compound 17 was attributed to the higher Pd loading and specific surface area. It is worth noting that Pd states immobilized on different support can also affect the catalytic activity.

To find the most active morphology, the effect of the nature of the carbon shell on the MNPs was investigated by examining three different shells. First, compounds 13 and 16 in Figure 2 were prepared by coating tetrahedral MNPs with melamine–formaldehyde polymer and glucose-derived carbon followed by palladating and carbonization. As tabulated, compound 13, in which the carbon shell is nitrogen rich, showed higher catalytic activity than compound 16, in which the carbon shell is nitrogen

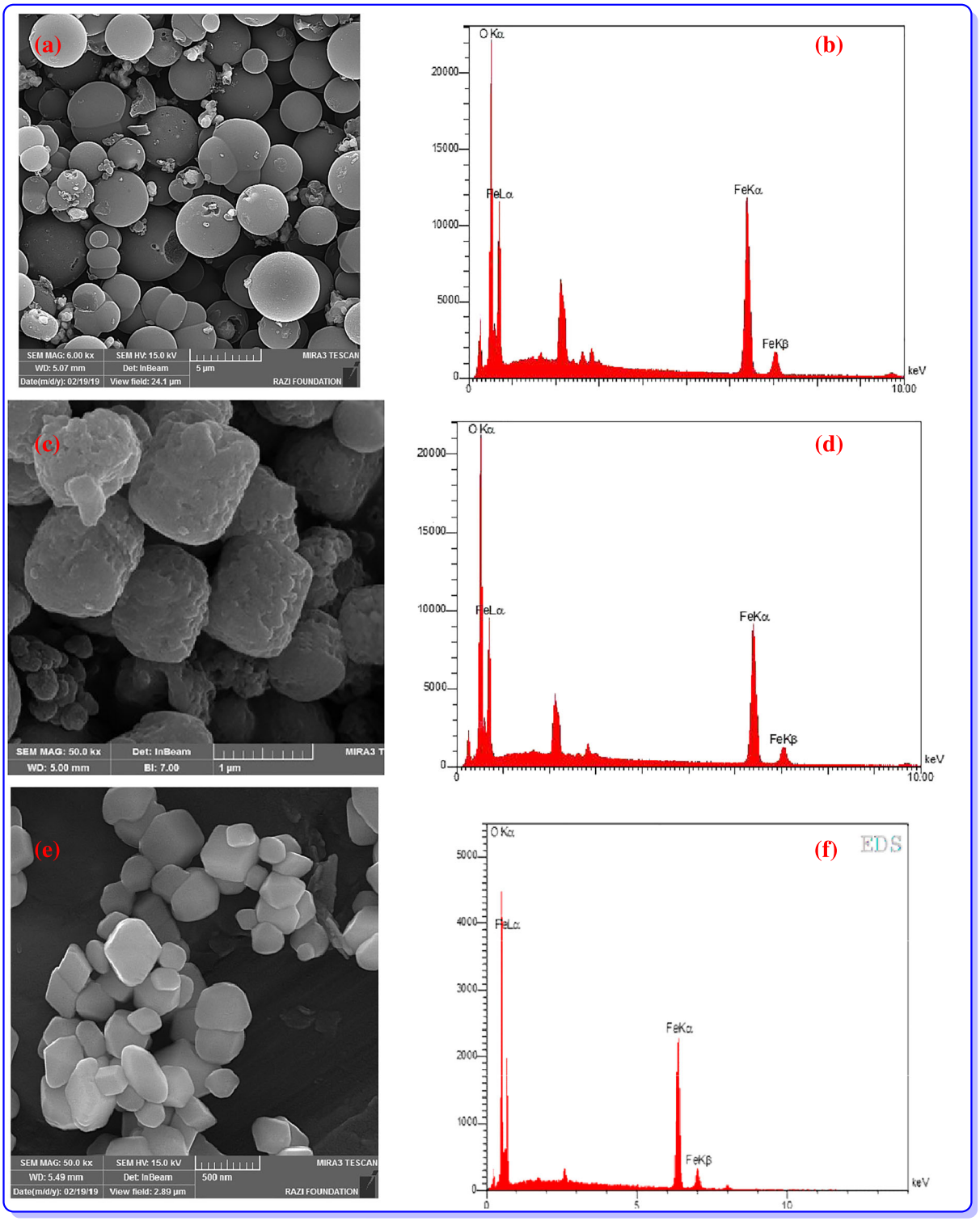

FIGURE 3 Field emission scanning electron microscopic and energy-dispersive X-ray spectroscopy analyses of h-Fe_2O_3 with (a,b) disc-like morphology, (c,d) cylinder morphology, and (e,f) tetrahedral morphology

TABLE 1 Comparison of the catalytic activity of the present catalyst with the other prepared catalysts for the hydrogenation reaction[a]

Entry	Catalyst	Yield[b] (%)	Time (min)	Loading of Pd nanoparticles (mmol/g)	S_{BET} (m^2 g^{-1})
1	Compound **7**	45	75	0.021	75
2	Compound **9**	30	75	0.013	64
3	Compound **17**	65	75	0.028	78
4	Compound **5**	100	75	0.06	451
5	Compound **11**	85	75	0.047	155
6	Compound **13**	80	75	0.041	124
7	Compound **16**	68	75	0.033	92

[a]Reaction condition: nitrobenzene (1 mmol), catalyst (1.2 mol%) in water (5 mL) at room temperature (under 1 atmosphere H_2 gas).

[b]Isolated yield.

free. This observation can be justified based on the capability of N-rich carbon shell to effectively anchor Pd nanoparticles through electrostatic interactions.

Again, ICP analysis was exploited to verify this assumption. As shown in Table 1, the Pd loading in compound 13 was higher than that in compound 16, confirming the role of the nature of the carbon shell and its nitrogen functionalities in the catalytic activity of the resulting catalyst. Notably, the BET results confirmed that the specific surface area of compound 13 was higher than that of compound 16. This can also contribute to the catalytic activity through improving the dispersion of Pd nanoparticles on the support. To further investigate the effect of carbon shell, another catalyst, compound 3, with combinatory carbon shell was prepared through initial coating of MNPs with melamine–formaldehyde followed by introduction of a secondary shell (Glu) through hydrothermal treatment of glucose. Compound 3 was then palladated and carbonized to furnish compound 5. Interestingly, use of compound 5 as a catalyst for the hydrogenation of nitrobenzene indicated the superior catalytic activity of this sample. The ICP analysis of this compound implied the highest loading of Pd in this nanocomposite, indicating that the dual shell was more effective for anchoring of Pd nanoparticles. Moreover, the BET results showed the high specific surface area of this sample that was significantly higher than that of compounds 13 and 16. Taking these results into account, the high catalytic activity of compound 5 can be attributed to its high specific surface area and Pd loading.

Finally, to elucidate the role of the order of Pd loading in the catalytic activity, another control catalyst, compound 11, was prepared through a similar protocol that was used for the preparation of compound 5, except that Pd loading was carried out at the final stage and after carbonization of the shell. The results (Table 1) showed that the catalytic activity, specific surface area, and Pd loading of this sample were higher than those of compounds 7, 9, 17, and 13, but lower than those of compound 5. This result indicated the importance of the order of Pd incorporation.

3.2 | Characterization of the catalyst of the choice, compound 5

In the previous section the Pd loading and specific surface area of all the control catalysts were measured. In the next step, compound 5 that showed the best catalytic activity was further characterized. First, the morphology of compound 5 was disclosed by recording the FESEM image (Figure 4). As shown in Figure 4, although coating with carbon shell disordered the morphology of the MNPs, to some extent, the tetrahedral morphology is still observable. The observation of C and N atoms in the EDS analysis of the catalyst confirmed the incorporation of N-doped carbon shell. Moreover, the presence of Pd in this analysis confirmed the successful immobilization of Pd nanoparticles.

The TEM images of the catalyst are illustrated in Figure 5, in which the large MNPs can be seen covered with carbon shell. On the carbon shell, the Pd nanoparticles with average size of 20 nm can be observed.

To further characterize the nature of the carbon shell of the catalyst, Raman spectroscopy was applied (Figure 6). The observation of two characteristic D and G bands at 1359 and 1594 cm^{-1} is a proof for the graphitic nature of the carbon shell.[34–36]

The porous nature of the catalyst was confirmed by BET analysis. As depicted in Figure 7, the N_2 adsorption–desorption isotherm of the catalyst is of type IV, implying its porous nature. In addition, the specific surface area of the catalyst was estimated to be 416 m^2 g^{-1}. According to the Barrett–Joyner–Halenda (BJH) plot, the pore-size distribution of Pd@TH-Fe_2O_3@MFC is narrow and the mesoporous size distribution centered at 2.4 nm. The total pore volume of the catalyst was estimated to be 35.8 m_3 g^{-1}. To understand the effect of covering MNPs with carbon shell, the specific surface area of compounds 1, 3, and 4 was also calculated and compared with that of the catalyst, compound 5. The results showed that the bare MNPs had a low specific surface area (51.4 m^2 g^{-1}). Upon covering the surface of MNPs with melamine–formaldehyde and glucose-derived carbon sheet, this value increased to 362 m^2 g^{-1}. The specific surface area of compound 4 (319 m^2 g^{-1}) was lower than that of Pd-free compound 3. This observation confirms that the Pd nanoparticles are deposited on the surface of

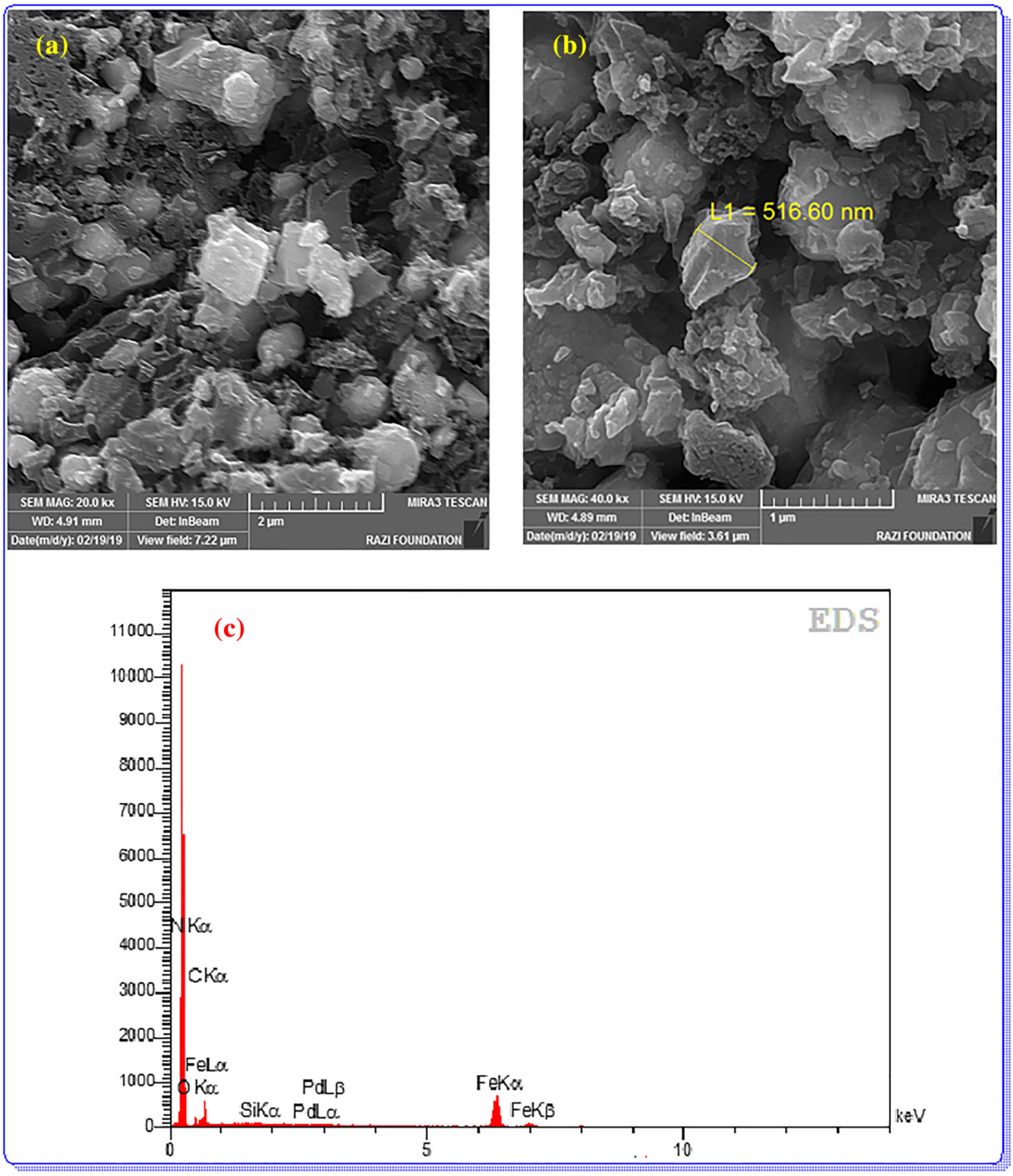

FIGURE 4 The (a,b) field emission scanning electron microscopic and (c) energy-dispersive X-ray spectroscopy (EDS) analyses of compound 5

compound 3. Finally, upon carbonization, the specific surface area showed an increase and reached to 416 $m^2\ g^{-1}$. This can be due to the formation of porous carbon with high specific surface area.

To verify the formation of MNPs and Pd nanoparticles, the XRD pattern of the catalyst was also obtained (Figure 8). As shown, the XRD pattern of the catalyst contains several characteristic bands. First, a broad band at 2θ = 20–27° is observable that can be attributed to the graphite-like carbon shell on the structure of the catalyst.[37] The second group of the characteristic bands is related to the Pd nanoparticles (observed at 2θ = 40°, 49°, 68°, 82.1°, and 86°). The third group of the characteristic bands can be attributed to the MNPs (observed at 2θ = 30.3°, 35.6°, 43.2°, 54.0°, 57.3°, 63.0°, and 74.6°; JCPDS card no. 39–1346).[6,38]

To further characterize the catalyst, FTIR spectroscopy was performed. In the FTIR spectrum of the catalyst

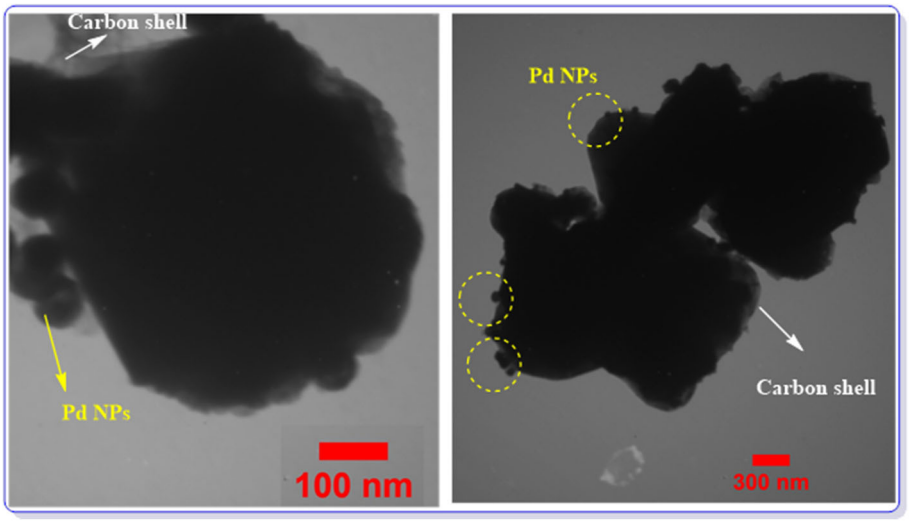

FIGURE 5 Transmission electron microscopy images of Pd@TH-Fe_2O_3@MFC. NP, nanoparticle

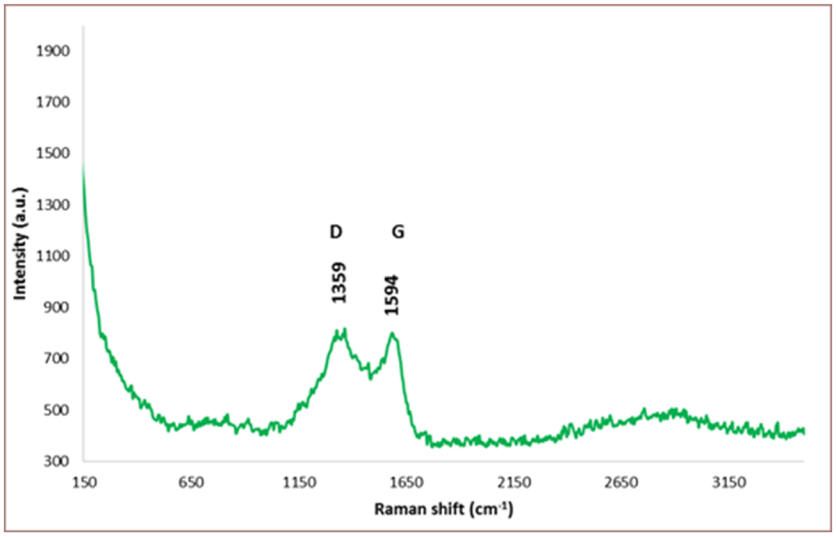

FIGURE 6 Raman spectrum of compound 5 (Pd@TH-Fe_2O_3@MFC)

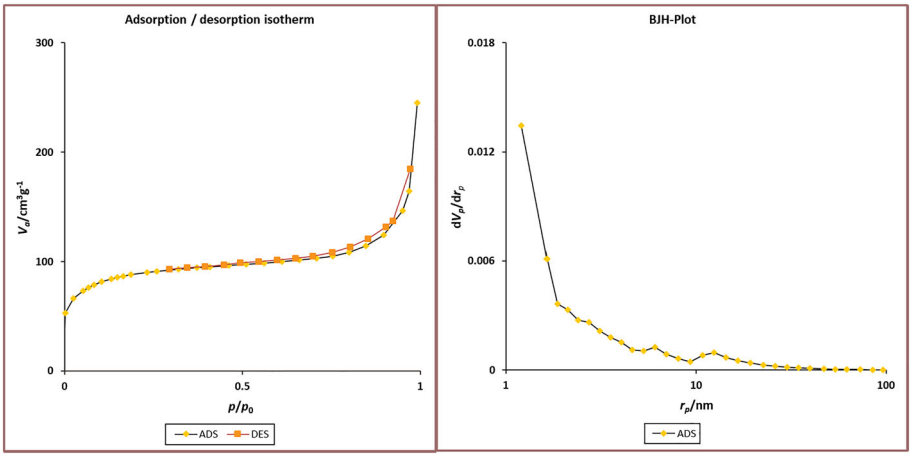

FIGURE 7 Nitrogen adsorption–desorption (ADS–DES) isotherm and Barrett–Joyner–Halenda (BJH) plot of Pd@TH-Fe_2O_3@MFC

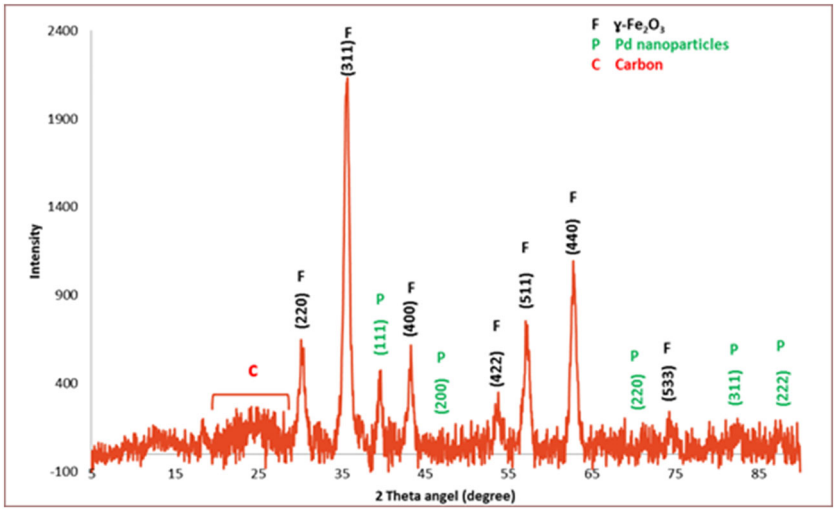

FIGURE 8 X-ray diffraction pattern of Pd@TH-Fe_2O_3@MFC

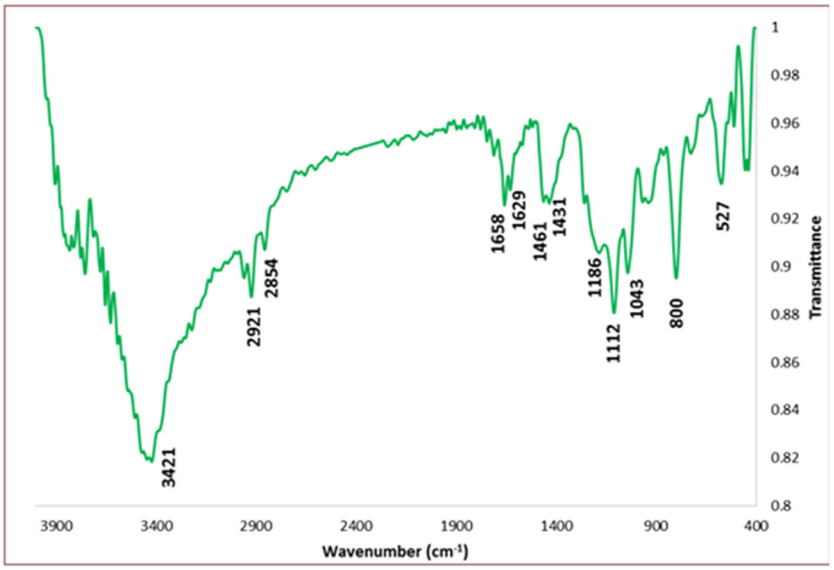

FIGURE 9 Fourier-transform infrared spectrum of compound 5 (Pd@TH-Fe_2O_3@MFC)

(Figure 9) the observed bands at 450–560 cm^{-1} can prove the Fe–O stretching vibration.[38] The presence of hydroxyl group can be confirmed by observing a broad band at 3421 cm^{-1}. The characteristic bands at 1658 and 1629 cm^{-1} can be attributed to the –C=N and –C=C functionalities, respectively, in the carbon shell on the periphery of MNPs.

Next, the magnetic property of compound 5 was studied by room-temperature VSM analysis. The measured maximum saturation magnetization (*Ms*) value of Pd@TH-Fe_2O_3@MFC was estimated to be 25.78 emu g^{-1} (Figure 10), which was lower than that of bare MNPs (45.28 emu g^{-1}). The relatively low *Ms* value can be assigned to the presence of carbon shell on the periphery of MNPs.[39] It is worth noting that although the non-magnetic carbon shell decreased the magnetic feature of the catalyst, it was still magnetic enough to be separated magnetically by using an external magnet. To further investigate the effect of the nature of the carbon shell on the magnetic properties of the final catalyst, VSM analysis of compounds 16 (the sample without the melamine–formaldehyde shell) and 13 (the sample without glucose-derived carbon) was performed. The results showed that similar to Pd@TH-Fe_2O_3@MFC, the *Ms* values of compounds 16 and 13 were lower than that of bare MNPs. However, the magnetic properties of these samples (37.8 and 36.0 emu g^{-1}, respectively) that possessed only one shell were higher than that of Pd@TH-Fe_2O_3@MFC that contained both melamine–formaldehyde and glucose-derived carbon shells. Moreover, the comparison of this value for both samples confirmed that the nature of carbon shell had an insignificant effect on the magnetic property of the catalyst and the *Ms* values of compounds 16 and 13 were very similar (37.8 and 36.0 emu g^{-1}, respectively).

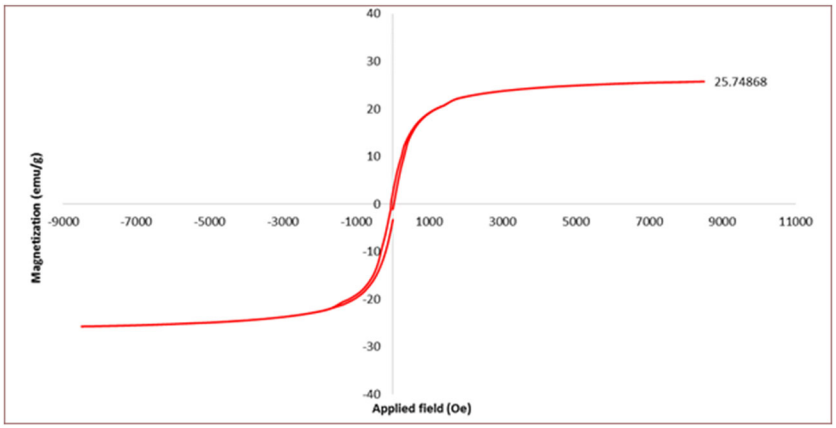

FIGURE 10 Vibrating-sample magnetometry analysis of compound 5

3.3 | Generality of the developed protocol

Notably, Pd@TH-Fe_2O_3@MFC not only could promote the hydrogenation of nitrobenzene, but also could effectively catalyze the hydrogenation of steric 1-nitronaphthalene (Table 2, entry 2) and NO_2-substituted aromatic ketones (Table 2, entry 3) selectively. Moreover, the hydrogenation of electron-withdrawing and electron-donating nitrobenzenes (Table 2, entries 4 and 5) resulted in the corresponding anilines with moderate yields in longer reaction times.

To show the merit of Pd@TH-Fe_2O_3@MFC, its catalytic activity for the hydrogenation of nitrobenzene was compared with some of the Pd-based catalysts reported in the literature. In Table 3, the efficiency of the previously reported catalysts and the reaction details such as reaction time, temperature, solvent, and reducing agent are summarized. As tabulated, a diverse range of Pd-based catalysts have been utilized for promoting this reaction. In some protocols, the chemical reducing agents were applied. Despite the efficiency of the chemical reducing agent, use of hydrogen gas is more appealing due to the environmental concerns. By contrast, in some of the H_2-assisted procedures, high pressures of hydrogen gas were used that are not only costly, but also unsafe. Regarding the reaction solvent and temperature, use of water as green and available solvent and performing the reaction at room temperature are more economical and environmentally benign. Comparing the reaction times, it can be seen that Pd@TH-Fe_2O_3@MFC could promote the reaction in reasonable reaction time. Considering all of the results, it can be concluded that Pd@TH-Fe_2O_3@MFC can be considered as an efficient catalyst for the hydrogenation of nitroarenes.

TABLE 2 Pd@TH-Fe_2O_3@MFC catalyzed hydrogenation of nitro arenes[a]

Entry	Reagent	Product	Time (h:min)	Yield[b] (%)
1	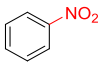	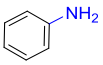	1:15	100
2	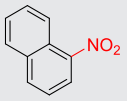	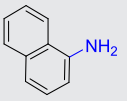	3:00	90
3	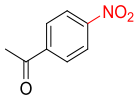	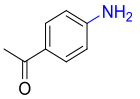	2:00	94
4	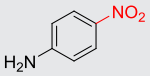	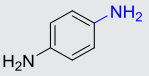	2:25	70
5	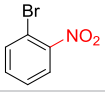	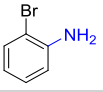	3:13	65

[a]Reaction condition: Nitro arene (1 mmol), Pd@TH-Fe_2O_3@MFC (1.2 mol%) in water (5 mL) at room temperature (under 1 atmosphere H_2 gas).

[b]Isolated yield.

3.4 | Catalyst recyclability

Recyclability of Pd@TH-Fe_2O_3@MFC for the hydrogenation of nitrobenzene was examined by repeating the recovery–reusing cycle for 10 consecutive reaction runs under similar hydrogenation conditions (Figure 11). As illustrated in Figure 11, Pd@TH-Fe_2O_3@MFC exhibited excellent catalytic activity and recycling up to four reaction runs and only an insignificant decrease of aniline yield was observed upon each recycling. Upon further recycling, the decrease of the yield of the reaction increased and upon recycling for 10 reaction runs, 32% loss of the catalytic activity was observed. From a structural point of view, the FTIR spectroscopy of the recycled catalyst confirmed that recycling did not induce significant change in the structure of the catalyst and both fresh and recycled Pd@TH-Fe_2O_3@MFC for 10 reaction runs showed similar FTIR spectra (Figure 12).

Finally, the Pd leaching of the catalyst after 10 reaction runs was measured and compared with that of control

TABLE 3 Comparison of the catalytic activities of Pd@TH-Fe_2O_3@MFC with some of the reported catalysts in the literature for the hydrogenation of nitrobenzene

Entry	Catalyst	Reducing agent	Time (h:min)	Temperature (°C)	Solvent	Yield (%)	Ref.
1	Pd@TH-Fe_2O_3@MFC (1.2 mol%)	H_2/1 atm	1:15	r.t.	H_2O	100	This work
2	Pd@Hal/di-urea[a] (1.5 wt%)	H_2/1 bar	1:00	50	H_2O	100	[40]
3	PdNP(0.5%)/Al_2O_3 (0.3 g)	H_2/1 atm	3:00	r.t.	THF	100	[41]
4	Pd/PPh_3@FDU-12[b] (8.33×10^{-4} mmol Pd)	H_2/10 bar	1:00	40	EtOH	99	[42]
5	Pd-$(CH_3)_2NHBH_3$ (6 mol%)	$(CH_3)_2NHBH_3$	0:10	r.t.	H_2O/MeOH	99	[43]
6	APSNP[c] (1 mol%)	H_2/40 atm	2:00	r.t.	EtOH	100	[44]
7	Pd/graphene	$NaBH_4$	1:30	50	H_2O/EtOH	91	[45]
8	Pd0-AmP-MCF[d] (0.5 mol%)	H_2/1 bar	1.15	r.t	EtOAc	90	[46]
9	PdNP@PPh_2-PEGPIILP[e] (0.05 mol%)	$NaBH_4$	2:00	r.t.	H_2O	99	[47]
10	Pd NPs/RGO (6 mg)	$NaBH_4$	1:30	50	H_2O/EtOH	98	[48]
11	PdCu/graphene (2 mol% Pd)	$NaBH_4$	1:30	50	H_2O/EtOH	98	[45]
12	PdCu/C (2 mol% Pd)	$NaBH_4$	1:30	50	H_2O/EtOH	85	[45]

[a]Pd immobilized on functionalized Hal.

[b]Pd nanoparticles (1.1 nm) with triphenylphosphine (PPh_3) cross-linked in the nanopore of FDU-12.

[c]Activated palladium sucrose nanoparticles

[d]Pd nanoparticles supported on aminopropyl-functionalized siliceous mesocellular foam.

[e]Palladium nanoparticles stabilized by lightly cross-linked phosphine-decorated polymer immobilized ionic liquids and their PEGylated counterparts (PEGPIIL).

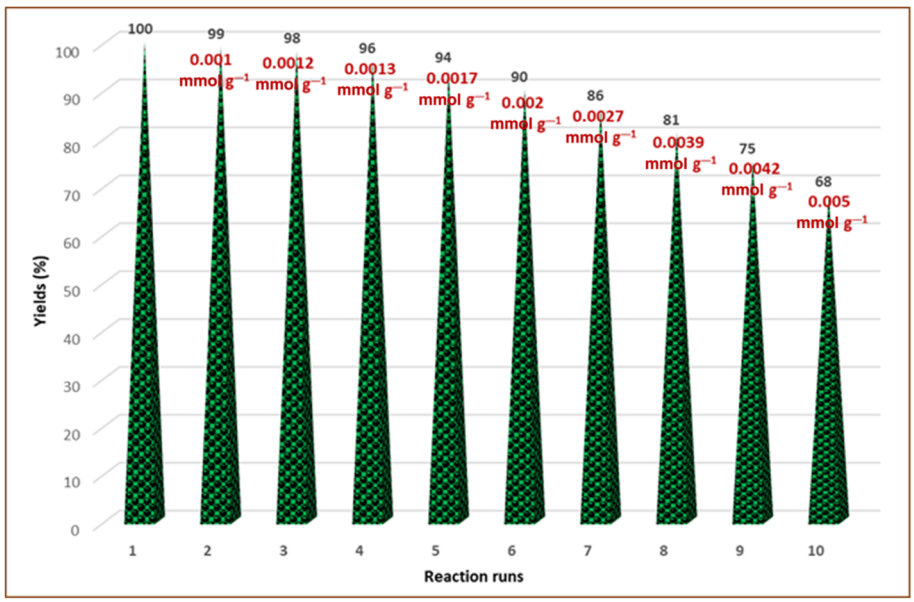

FIGURE 11 Yield of aniline after each run of recycling the Pd@TH-Fe_2O_3@MFC catalyst and the Pd leaching

catalysts (Table 4). As tabulated, the bare samples (compounds 7, 9, and 17) that do not have any shell showed higher Pd leaching compared with that of the encapsulated ones. By comparing the Pd leaching of the sample with glucose-derived carbon shell with that of the sample with melamine–formaldehyde shell (compounds 13 and 16), it was confirmed that the N-rich shell suppresses the Pd leaching more effectively. This can be attributed to the interactions of the heteroatoms in carbon shell with Pd nanoparticles. The measurement of Pd leaching of compound 11 with that of 5 showed that the order of Pd loading did not affect the Pd leaching significantly and both of the catalysts showed similar leaching (0.005 mmol g^{-1}).

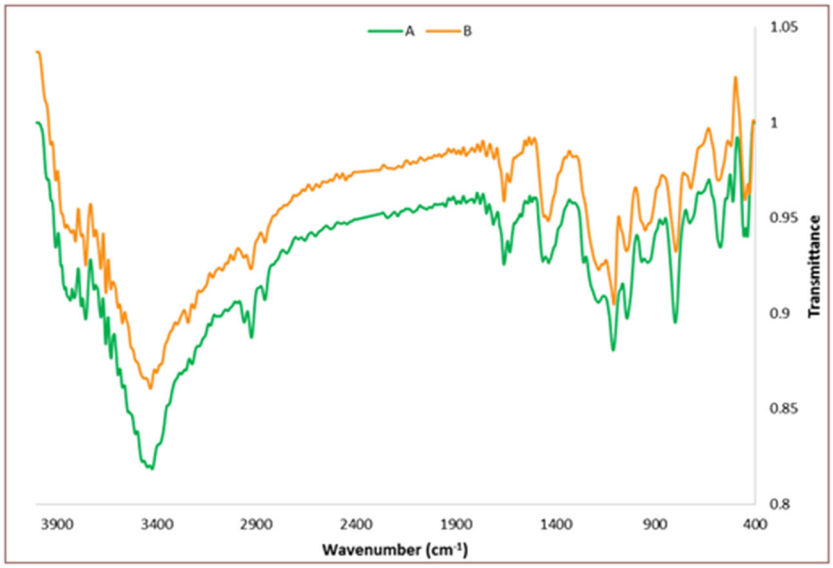

FIGURE 12 Fourier-transform infrared spectra of A: fresh and B: recycled Pd@TH-Fe_2O_3@MFC after 10 runs

TABLE 4 Comparison of the Pd leaching of the catalyst and control samples after 10 reaction runs[a]

Entry	Catalyst	Leaching of Pd nanoparticles (mmol/g)
1	Compound **7**	0.012
2	Compound **9**	0.0092
3	Compound **17**	0.008
4	Compound **5**	0.005
5	Compound **11**	0.005
6	Compound **13**	0.0062
7	Compound **16**	0.0069

[a]Reaction condition: nitrobenzene (1 mmol), catalyst (1.2 mol%) in water (5 mL) at room temperature (under 1 atmosphere. H_2 gas).

4 | CONCLUSION

To investigate the effects of structural parameters on the catalytic activity of magnetic core–shell catalyst, three MNPs with three different morphologies, disc-like, cylinder, and tetrahedral, were prepared and used as Pd nanoparticles support. The results showed that the morphology can affect the specific surface area and Pd loading and leaching of the final catalyst, with the tetrahedral morphology identified as the best choice, as it had the highest catalytic activity for the hydrogenation of nitrobenzene. To improve the catalytic activity of the catalyst and prevent the catalyst from aggregation of MNPs, the catalyst was covered by a dual shell by introduction of melamine–formaldehyde shell, followed by coating with glucose-derived carbon. The Pd immobilization and carbonization led to a catalyst, Pd@TH-Fe_2O_3@MFC, with excellent catalytic activity and recyclability. To study the effect of the nature of shell on the catalytic activity, some control samples with N-rich carbon derived from melamine–formaldehyde and N-free glucose-derived carbon were also prepared and their catalytic activities were compared with that of Pd@TH-Fe_2O_3@MFC. The results confirmed the higher catalytic activity of the latter. This was attributed to the higher specific surface area and Pd loading of this sample. Examining the effect of the order of Pd immobilization showed that incorporation of Pd prior to carbonization was more effective than after thermal treatment.

ACKNOWLEDGMENTS

The authors appreciate the partial supports from the Iran Polymer and Petrochemical Institute and Alzahra University. S. Sadjadi and Heravi thank Iran National Science Foundation (INSF) for the Individual given grant (No. 97009384). M. Malmir's contribution is also appreciated.

CONFLICT OF INTEREST

There are no conflicts to declare. The Iranian authors declare that none of them are employed by a government agency that has a primary function other than research and/or education. Moreover, none of them are official representative or on behalf of the government.

ORCID

Samahe Sadjadi https://orcid.org/0000-0002-6884-4328
Majid M. Heravi https://orcid.org/0000-0003-2978-1157

REFERENCES

[1] G. Han, X. Li, J. Li, X. Wang, Y. S. Zhang, R. Sun, *ACS Omega* **2017**, *2*, 4938.

[2] X. Zhang, Y. Niu, Y. Yang, Y. Li, J. Zhao, *New J. Chem.* **2014**, *38*, 4351.

[3] T. Zare, N. Sattarahmady, *Clin. Cancer Res.* **2015**, *7*, 29.

[4] S. Sadjadi, M. M. Heravi, M. Malmir, *J. Taiwan Inst. Chem. Eng.* **2018**, *86*, 240.

[5] C. Jin, Y. Wang, H. Tang, K. Zhu, X. Liu, J. Wang, *J. sol-Gel Sci. Technol.* **2016**, *77*, 279.

[6] S. Sadjadi, M. Malmir, M. M. Heravi, *RSC Adv.* **2017**, *7*, 36807.

[7] W. Zhou, L. Guo, *Chem. Soc. Rev.* **2015**, *44*, 6697.

[8] W. Wu, Q. He, C. Jiang, *Nanoscale Res. Lett.* **2008**, *3*, 397.

[9] S. Kazemi Movahed, N. Farajinia Lehi, M. Dabiri, *J. Catal.* **2018**, *364*, 69.

[10] Y. Yang, X. Jiang, J. Chao, C. Song, B. Liu, D. Zhu, Y. Sun, B. Yang, Q. Zhang, Y. Chen, L. Wang, *Sci. China Mater.* **2017**, *60*, 1129.

[11] J. K. Shon, X. Jin, Y. S. Choi, J. G. Won, Y. K. Hwang, D. J. You, C. Li, J. M. Kim, *Carbon Lett.* **2016**, *20*, 66.

[12] Z. Z. Jiang, Z. B. Wang, H. Rivera, W. L. Qu, D. M. Gu, *Fuell Cells* **2014**, *14*, 660.

[13] T. A. Centeno, A. B. Fuertes, *J. Membr. Sci.* **1999**, *160*, 201.

[14] G. Han, X. Wang, J. Hamel, H. Zhu, R. Sun, *Sci. Rep.* **2016**, *6*, 38164.

[15] Z. Shen, Y. Luo, Q. Wang, X. Wang, R. Sun, *ACS Appl. Mater. Interfaces* **2014**, *6*, 16147.

[16] M. Mastalerz, *Angew. Chem. Int. Ed.* **2008**, *47*, 445.

[17] F. J. Uribe-Romo, J. R. Hunt, H. Furukawa, C. Klöck, M. O'Keeffe, O. M. Yaghi, *J. Am. Chem. Soc.* **2009**, *131*, 4570.

[18] G. A. Zaharias, H. H. Shi, S. F. Bent, *Thin Solid Films* **2006**, *501*, 341.

[19] J. Du, F. Cheng, S. Wang, T. Zhang, J. Chen, *Sci. Rep.* **2014**, *4*, 4386.

[20] Y. Zhao, K. Watanabe, K. Hashimoto, *J. Am. Chem. Soc.* **2012**, *134*, 19528.

[21] I. Ghiviriga, D. C. Oniciu, *Chem. Commun.* **2002**, *22*, 2718.

[22] J. S. Lee, G. S. Park, S. T. Kim, M. Liu, J. Cho, *Angew. Chem. Int. Ed.* **2013**, *52*, 1026.

[23] X. Lin, X. Li, F. Li, Y. Fang, M. Tian, X. An, Y. Fu, J. Jin, J. Ma, *J. Mater. Chem. A* **2016**, *4*, 6505.

[24] N. B. McKeown, P. M. Budd, *Chem. Soc. Rev.* **2006**, *35*, 675.

[25] J. H. Wang, Z. L. Yuan, R. F. Nie, Z. Y. Hou, X. M. Zheng, *Ind. Eng. Chem. Res.* **2010**, *49*, 4664.

[26] P. Lara, K. Philippot, *Cat. Sci. Technol.* **2014**, *4*, 2445.

[27] Z. Y. Sun, Y. F. Zhao, Y. Xie, R. T. Tao, H. Y. Zhang, C. L. Huang, Z. M. Liu, *Green Chem.* **2010**, *12*, 1007.

[28] B. N. Saïb, P. Grange, P. Verhasselt, F. Addoun, V. Dubois, *Appl. Catal. A* **2005**, *286*, 74.

[29] N. Arora, A. Mehta, A. Mishra, S. S. Basu, *App. Clay Sci.* **2018**, *151*, 1.

[30] Y. Chen, L. Li, L. Zhang, J. Han, *Colloid Polym. Sci.* **2018**, *296*, 567.

[31] F. Figueras, B. Coq, *J. Mol. Catal. A: Chem.* **2001**, *173*, 223.

[32] M. Liu, J. Zhang, J. Liu, W. W. Yu, *J. Catal.* **2011**, *278*, 1.

[33] M. Liu, W. Yu, H. Liu, *J. Mol. Catal. A: Chem.* **1999**, *138*, 295.

[34] J. Hou, C. Cao, F. Idrees, X. Ma, *ACS Nano* **2015**, *9*, 2556.

[35] F. Yang, Z. Zhang, K. Du, X. Zhao, W. Chen, Y. Lai, J. Li, *Carbon* **2015**, *91*, 88.

[36] A. Esmaeili, M. H. Entezari, *J. Colloid Interface Sci.* **2014**, *432*, 19.

[37] B. Manoj, A. G. Kunjomana, *IOP Conf. Ser.: Mater. Sci. Eng.* **2015**, *73*, 1.

[38] A. Elhampour, M. Malmir, E. Kowsari, F. Boorboor Ajdari, F. Nemati, *RSC Adv.* **2016**, *6*, 96623.

[39] S. Sadjadi, M. M. Heravi, M. Malmir, *Appl. Organomet. Chem.* **2018**, *32*, e4029.

[40] S. Dehghani, S. Sadjadi, N. Bahri-Laleh, M. Nekoomanesh-Haghighi, A. Poater, *Appl. Organomet. Chem.* **2019**, *33*, e4891.

[41] S. Agrahari, S. Lande, V. Balachandran, G. Kalpana, R. Jasra, *J. Nanosci. Curr. Res.* **2017**, *2*, 2572.

[42] M. Guo, H. Li, Y. Ren, X. Ren, Q. Yang, C. Li, *ACS Catal.* **2018**, *8*, 6476.

[43] N. M. Patil, M. A. Bhosale, B. M. Bhanage, *RSC Adv.* **2015**, *5*, 86529.

[44] D. Samsonu, M. Brahmayya, B. Govindh, Y. Murthy, *S. Afr. J. Chem. Eng.* **2018**, *25*, 110.

[45] Y.-S. Feng, J.-J. Ma, Y.-M. Kang, H.-J. Xu, *Tetrahedron* **2014**, *70*, 6100.

[46] O. Verho, K. P. Gustafson, A. Nagendiran, C. W. Tai, J. E. Bäckvall, *ChemCatChem* **2014**, *6*, 3153.

[47] S. Doherty, J. Knight, T. Backhouse, A. Bradford, F. Saunders, R. Bourne, T. Chamberlain, R. Stones, A. Clayton, K. Lovelock, *Cat. Sci. Technol.* **2018**, *8*, 1454.

[48] M. Nasrollahzadeh, S. M. Sajadi, A. Rostami-Vartooni, M. Alizadeh, M. Bagherzadeh, *J. Colloid Interface Sci.* **2016**, *466*, 360.

SUPPORTING INFORMATION

Additional supporting information may be found online in the Supporting Information section at the end of the article.

How to cite this article: Sadjadi S, Heravi MM. Pd@tetrahedral hollow magnetic nanoparticles coated with N-doped porous carbon as an efficient catalyst for hydrogenation of nitroarenes. *Appl Organometal Chem*. 2019;e5229. https://doi.org/10.1002/aoc.5229